Importance of Nonadiabatic Effects in Kohn Anomalies in 1D Metals

Enrico Marazzi,[1,*] Samuel Poncé,[2,3] Jean-Christophe Charlier,[1] and Gian-Marco Rignanese[2,3,4,†]
[1]Institute of Condensed Matter and Nanosciences, Université catholique de Louvain, Chemin des Étoiles 8, B-1348 Louvain-la-Neuve, Belgium
[2]European Theoretical Spectroscopy Facility, Institute of Condensed Matter and Nanosciences, Université catholique de Louvain, Chemin des Étoiles 8, B-1348 Louvain-la-Neuve, Belgium
[3]WEL Research Institute, Avenue Pasteur, 6, 1300 Wavre, Belgium
[4]School of Materials Science and Engineering, Northwestern Polytechnical University, No. 127 Youyi West Road, Xi'an 710072 Shaanxi, People's Republic of China

(Received 23 June 2025; revised 26 September 2025; accepted 25 November 2025; published 17 December 2025)

Kohn anomalies are kinks or dips in phonon dispersions which are pronounced in low-dimensional materials. We investigate the effects of nonadiabatic phonon self-energy on Kohn anomalies in one-dimensional metals by developing a model that analyzes how the adiabatic phonon frequency, electron effective mass, and electron-phonon coupling strength influence phonon mode renormalization. We introduce an electron-phonon coupling strength threshold for low-temperature system instability, providing experimentalists with a tool to predict them. Finally, we validate the predictions of our model against first-principles calculations on a 4 Å-diameter carbon nanotube.

DOI: 10.1103/x69r-8fw1

Kohn anomalies (KAs) are softening of phonon modes in particular portions of the Brillouin zone (BZ) [1]. In Kohn's seminal work, the origin of this phenomenon was attributed to the screening of lattice vibrations by the excitation of electrons at the Fermi surface (FS). Soon after this theoretical prediction, KAs were observed by inelastic neutron scattering in lead [2]. Subsequently, they were seen in other metals [3–5], superconductors [6,7], and various other materials [8,9]. For a long time, the common belief was that electron and lattice dynamics were independent and that phonon instabilities were due solely to electronic effects [10]. However, this is only true for pure one-dimensional (1D) metals where the electronic response function diverges for the $\mathbf{q}$ vectors connecting points in the FS, called perfect FS nesting. In quasi-1D, two-dimensional (2D), and three-dimensional (3D) materials, the electronic response function does not exhibit such divergence [11]. For 2D and 3D systems, the situation is complicated by the fact that phonon softening occurs at $\mathbf{q}$ vectors which are incommensurate with perfect FS nesting vectors [12]. It was therefore suggested that the origin of KAs lies in the electron-phonon coupling (EPC), since electronic and lattice instabilities always occur simultaneously. FS nesting contributes to creating instabilities, but is not the only driving force.

In this framework, recent computational efforts have focused on improving the accuracy of phonon dispersion in metals. One method incorporates anharmonic corrections to the phonon dispersion relations [13], while another accounts for nonadiabatic (NA) effects due to EPC [14–16], supporting the idea that EPC lies at the heart of these instabilities. However, the impact of NA effects on 1D systems remains unclear, which complicates the assessment of phonon mode softening. Another open question is to identify the physical conditions that drive the instability.

In this Letter, we develop a 1D model to show that a minimum EPC strength is required to yield an imaginary phonon frequency, demonstrating that even a 1D metal can remain dynamically stable under conditions of perfect FS nesting when a nonadiabatic description is adopted. This threshold depends only on the adiabatic phonon frequency $\omega_{\mathbf{q}\nu}$ and the electron effective mass m^*; it decreases as $\omega_{\mathbf{q}\nu}$ decreases and m^* increases. As such, the threshold provides a simple predictive tool for identifying low-temperature structural instabilities experimentally. Finally, we perform first-principles calculations on a 4 Å-diameter carbon nanotube and find good agreement with our model.

In first-principles computations, phonon frequencies are usually calculated using density functional perturbation theory (DFPT) [17,18] within the adiabatic approximation. They are obtained by diagonalizing the DFPT dynamical matrix D^{DFPT}, which is the sum of the bare dynamical matrix D^{b} and the static-adiabatic phonon self-energy Π^{A} [14],

$$D^{\mathrm{DFPT}}_{\mathbf{q}\nu\mu}(\omega=0,\sigma) = D^{\mathrm{b}}_{\mathbf{q}\nu\mu} + \Pi^{\mathrm{A}}_{\mathbf{q}\nu\mu}(\omega=0,\sigma), \quad (1)$$

where $\mathbf{q}$ is the phonon wave vector, ν and μ are phonon modes, ω is the vibrational dynamical variable, and σ is a

*Contact author: enrico.marazzi@uclouvain.be
†Contact author: gian-marco.rignanese@uclouvain.be

large electronic temperature, which acts as a smearing parameter. Here the σ is not intended to represent a physical temperature, but it is a numerical parameter used to ensure convergence in metallic systems. Going beyond DFPT to obtain the dynamical matrix D requires one to compute the nonadiabatic phonon self-energy Π^{NA},

$$D_{\mathbf{q}\nu\mu}(\omega,T) = D^{\mathrm{b}}_{\mathbf{q}\nu\mu} + \Pi^{\mathrm{NA}}_{\mathbf{q}\nu\mu}(\omega,T), \tag{2}$$

where T is the electronic temperature. The bare dynamical matrix can be difficult to compute in a pseudopotential *ab initio* framework [14] such that it is advantageous to compute D from D^{DFPT} by subtracting the static-adiabatic phonon self-energy and adding the dynamical nonadiabatic one:

$$D_{\mathbf{q}\nu\mu}(\omega,T) = D^{\mathrm{DFPT}}_{\mathbf{q}\nu\mu}(0,\sigma) - \Pi^{\mathrm{A}}_{\mathbf{q}\nu\mu}(0,\sigma) + \Pi^{\mathrm{NA}}_{\mathbf{q}\nu\mu}(\omega,T). \tag{3}$$

The dynamical NA phonon self-energy can be computed with two screened vertices as [14,19–22]

$$\Pi^{\mathrm{NA}}_{\mathbf{q}\nu\mu}(\omega,T) = \frac{2}{\hbar}\sum_{mn}\int \frac{d\mathbf{k}}{\Omega^{\mathrm{BZ}}} \times \left[g^{mn\mu}_{\mathbf{kq}}(0,\sigma)\right]^{*} \chi^{mn}_{\mathbf{kq}}(\omega,T) g^{mn\nu}_{\mathbf{kq}}(0,\sigma), \tag{4}$$

where $g^{mn\nu}_{\mathbf{kq}}(0,\sigma)$ are two screened EPC matrix elements, Ω^{BZ} is the Brillouin-zone volume, m and n are electron band indices, $\mathbf{k}$ is an electron wave vector, and $\chi^{mn}_{\mathbf{kq}}(\omega,T)$ is bare electronic susceptibility given by

$$\chi^{mn}_{\mathbf{kq}}(\omega,T) = \left[\frac{f_{m\mathbf{k}+\mathbf{q}}(T) - f_{n\mathbf{k}}(T)}{\varepsilon_{m\mathbf{k}+\mathbf{q}} - \varepsilon_{n\mathbf{k}} - \hbar(\omega + i\eta)}\right], \tag{5}$$

where f is the Fermi-Dirac (FD) distribution function, $\varepsilon_{n\mathbf{k}}$ the DFT electron eigenvalues, and η an infinitesimal quantity.

Here, we develop a 1D model with a parabolic electronic band ε_k crossing the FS and a single-phonon mode ν aiming to study the behavior of the phonon self-energy due to EPC. More details about this model can be found in Sec. S1 of Supplemental Material [23]. In this model, we assume a constant EPC $|g_Q|$ and a parabolic dispersion $\varepsilon_k = \hbar^2(k^2 - K^2)/2m^*$. Here, $K = k_{\mathrm{F}}$ is the Fermi wave vector that establishes the KA at $q = Q = 2K$. In the model, we exclude the indices n, m, and ν when they are not pertinent, for the sake of clarity. The assumption of a constant $|g_Q|$ is justified because the temperature dependence in Eq. (4) arises only from the FD distribution in Eq. (5); the validity of this approximation is discussed in Sec. S2 of Supplemental Material [23]. Therefore, this dependence has a contribution only from a small region around the Fermi level, where the EPC can be approximated as a constant. Since this approximation worsens at higher temperature, we focus on the low-temperature regime.

Using first-order perturbation theory, the NA correction results in a renormalization of the phonon frequency which can be evaluated by retaining the diagonal elements of the self-energy Π^{NA} only, as only one phonon branch is included in the model [14,20]:

$$\Omega^2_Q(T) = \omega^2_Q + \gamma^2_Q(\Omega_Q - i\gamma_Q, T) + 2\omega_Q \times \left[\mathrm{Re}\Pi^{\mathrm{NA}}_Q(\Omega_Q - i\gamma_Q, T) - \mathrm{Re}\Pi^{\mathrm{A}}_Q(0,\sigma)\right], \tag{6}$$

where Ω_Q is the renormalized phonon frequency, ω_Q the high-temperature adiabatic frequency that acts as the DFPT one, and γ_Q the phonon linewidth due to the EPC that can be expressed as

$$\gamma_Q(\Omega_Q - i\gamma_Q, T) = -\frac{\omega_Q}{\Omega_Q}\mathrm{Im}\,\Pi^{\mathrm{NA}}_Q(\Omega_Q - i\gamma_Q, T). \tag{7}$$

Equations (6) and (7) are solved self-consistently and we choose an initial value $\gamma_Q = 1$ meV. We confirm the robustness of the self-consistent solution for a broad range of initial guesses for γ_Q, see Sec. S3 of Supplemental Material [23]. The adiabatic self-energy $\mathrm{Re}\Pi^{\mathrm{A}}_Q(0,\sigma)$ is computed through Eq. (4) with $\omega = 0$ and $T = \sigma$. Additional details are provided in Sec. S4 of Supplemental Material [23]. Equation (6) differs from Eq. (139) of Ref. [20] because we use the alternative but equivalent definition of NA from Ref. [14]. Here, we define as NA everything that goes beyond D^b [Eq. (2)] so that we can explicitly define $\Pi^{\mathrm{NA}}_{\mathbf{q}\nu\mu}$ and $\Pi^{\mathrm{A}}_{\mathbf{q}\nu\mu}$ at two different temperatures, σ and T [Eq. (3)]. The approximation of considering the diagonal term only in Eq. (6) is exact in the model, as only one phonon branch is considered, but it is an approximation which usually gives good results also for real materials [20]. However, there are cases where this approximation fails, e.g., for semiconductors with narrow band gap [25].

In Fig. 1, we show the normalized solution to Eq. (6), defined as $\tilde{\Omega}_Q \equiv (\Omega_Q/\omega_Q)$, as a function of the normalized EPC matrix element:

$$|\tilde{g}_Q| \equiv \frac{|g_Q|}{|g_Q|_0}, \tag{8}$$

where $|g_Q|_0$ is the value of $|g_Q|$ such that Eq. (6) is verified for $\Omega_Q = 0$. The results presented in Fig. 1 are obtained at $T = 0$ K for which the integral in Eq. (4) can be computed analytically with a constant $|g_Q|$, as shown in Sec. S4 of Supplemental Material [23]. The smearing parameter is set to $\sigma = 6000$ K, approximately corresponding to 40 mRy, as this is a reasonable value used in DFT calculations for metals. In Fig. 1, different colors indicate different values of ω_Q, ranging from 10 to 200 meV, while the shaded area in the inset represents variations of m^* between 0.2 and 5.0. We limit the analysis to values of $0.2 < m^* < 5.0$ because

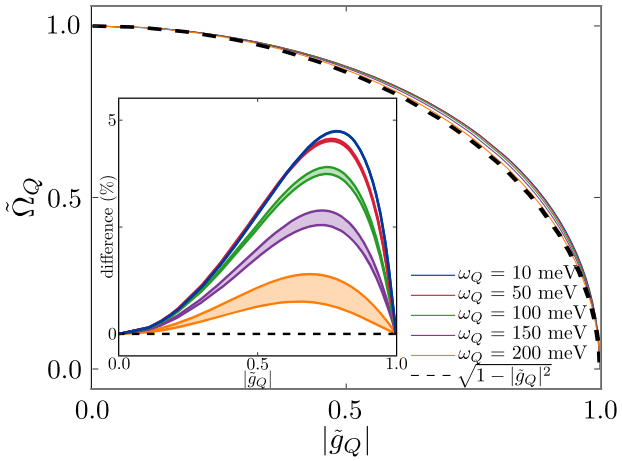

FIG. 1. Normalized phonon frequency Ω_Q as a function of the normalized EPC matrix element $|\tilde{g}_Q|$, defined in Eq. (8) at 0 K. Various values are reported for ω_Q: 10, 50, 100, 150, and 200 meV in blue, red, green, purple, and orange, respectively, with $m^* = 1$. The black dashed line is the reference circular arc. The inset shows the deviation from this perfectly circular curve. The color code is the same and the shaded area account for different m^* ranging between 0.2 and 5.0.

perturbation theory is expected to fail when the bands become too flat or too dispersive. Additionally, we limit ω_Q to values smaller than 200 meV as this is an upper bound for phonon frequencies in materials. The figure shows that the $\tilde{\Omega}_Q - |\tilde{g}_Q|$ relation closely follows a circular arc with a black dashed line. In the inset, the deviation from the perfect circular shape is shown as a function of $|\tilde{g}_Q|$ for different values of ω_Q and m^*. The shape of the $\tilde{\Omega}_Q$-$|\tilde{g}_Q|$ curve is affected by ω_Q and m^* in two different ways: a larger ω_Q brings the curve closer to a circular arc, but amplifies the influence of the effective mass.

Since the value of $|g_Q|$ required to obtain $\Omega_Q = 0$ remains finite even at $T = 0$ K, we can consider $|g_Q|_0$ as a lower bound for the EPC vertices leading to system instability. Therefore, being able to estimate the value of this threshold and compare it with the measured value of $|g_Q|$ is a tool to determine the stability of the system experimentally. For this purpose, we approximate

$$|g_Q|_0 \approx g_0 = \alpha + \beta \frac{\omega_Q^\delta}{(m^*)^\zeta}, \tag{9}$$

with $\alpha = 7.278$ meV, $\beta = 5.186$ meV$^{1-\delta}$, $\delta = 0.763$, and $\zeta = 0.518$, where the units of α and β ensure dimensional consistency. The parameters are computed by fitting Eq. (9) on $|g_Q|_0$ for different values of m^* and ω_Q. The approximation is validated in Sec. S5 of Supplemental Material [23], where the percentage difference between g_0 and $|g_Q|_0$ is shown as a function of ω_Q and m^*. Moreover, the agreement between the prediction of the model and the solution of Eq. (6) is discussed in Sec. S4 of Supplemental Material [23]. We find an overall good agreement but it worsen as ω_Q approaches 0 meV and when the electronic band becomes flat or too dispersive. Since g_0 depends only on ω_Q and m^*, it can be easily evaluated and compared with the experimental value of $|g_Q|$.

When $|g_Q| > g_0$, the renormalized frequency can become imaginary below a certain temperature. In contrast, when $|g_Q| < g_0$, the frequency at $q = Q$ always remains positive even if a dip also appears in the renormalized bandstructure. This can be shown analytically at $T = 0$ K where the integral in Eq. (4) yields [23]

$$\int \mathrm{d}k \chi_{kq}(\Omega_Q - i\gamma_Q, 0) = \frac{m^*}{2q} \log\left[\frac{(\Omega_Q^2 + \gamma_Q^2)^2}{\left(\left(\frac{q^2}{m^*} + \Omega_Q\right)^2 + \gamma_Q^2\right)\left(\left(\frac{q^2}{m^*} - \Omega_Q\right)^2 + \gamma_Q^2\right)}\right]. \tag{10}$$

Its substitution into Eq. (6) provides the value of $\Omega_Q(T = 0) > 0$. For $T > 0$ K, an analytical solution is no longer available for the integral of Eq. (4) but it can be computed numerically. In general, lower temperatures enhance the importance of the phonon frequency renormalization. However, as the temperature increases, Ω_Q first decreases, reaching a minimum before rising again to approach the adiabatic frequency at high temperature. Interestingly, when $|g_Q| \ll g_0$, Ω_Q reaches a minimum value at the temperature

$$T^{\min} = \frac{\omega_Q}{4.6 k_B}, \tag{11}$$

which does not depend on m^* as shown in Sec. S6 of Supplemental Material [23]. We also remark that when $|g_Q| \to g_0$, the renormalization effect is more pronounced. Therefore, for any 1D system, g_0 constitutes a threshold for the EPC strength above which the system becomes unstable at low temperature. It depends solely on ω_Q and m^* and Eq. (9) suggests that the threshold increases with larger ω_Q and smaller m^*. Therefore, we expect a system to be prone to instability if the adiabatic frequency is low and the effective mass large.

We evaluated the validity of our model by comparing it with first-principles calculations on the (3,3) carbon nanotube (CNT) and the boron and strained gold monoatomic chains. We use Quantum ESPRESSO [26–28] and EPW [29–31]

to compute the DFT electron bandstructures, the DFPT phonon frequencies, the EPC matrix elements, and the phonon self-energies. The local density approximation (LDA) is used with a plane-wave basis set of 100 Ry and a norm-conserving pseudopotential from Pseudo-Dojo [32], with stringent accuracy. The CNT is modeled in a hexagonal unit cell with the z axis aligned with the tube axis, and a 13 Å-vacuum along the off-axis directions to prevent spurious interactions between periodic replicas. Reciprocal space sampling is converged for each smearing temperature, with k grids ranging from $1\times1\times10^2$ to $1\times1\times10^4$, and q grids from $1\times1\times50$ to $1\times1\times200$. Electron bands and EPC matrix elements are interpolated using maximally localized Wannier functions [33,34] as implemented in EPW. Equation (4) is calculated using a broadening parameter $\eta = k_B T/100$ with uniform grids ranging from $1\times1\times10^4$ for $T = 1500$ K to $1\times1\times10^6$ for $T = 50$ K.

The (3,3) CNT [35,36] is a one-dimensional metal that can be synthesized using zeolite templates [37]. Its electronic bands structure shows a Dirac cone at $K \simeq 0.575\Gamma$-X. This band structure suggests a perfect FS nesting at $2(1-K)\simeq0.85\Gamma$-X. The electron and phonon band structures, computed with $\sigma = 10$ mRy and a cold smearing [38], are shown in Figs. 2(a) and 2(b), respectively. The phonon band structure shows a dip for three phonon modes at the expected position: the radial breathing mode (RBM) with an adiabatic $\omega_Q = 35.28$ meV, the in-plane longitudinal and transverse optical mode [$A_1(T)$ and $A_1(L)$] with $\omega_Q = 130.11$ and 143.42 meV, respectively. The DFPT frequencies, computed with a Fermi-Dirac smearing, are depicted in Figs. 2(d), 2(f), and 2(h), with a dotted line for the corresponding mode with $\sigma = T$, while the solid lines are computed through Eq. (6). Lowering the smearing parameter σ as a proxy for the temperature in the DFPT calculation, we observe that for the RBM the frequency becomes imaginary at ~220 K. For the $A_1(L)$ and $A_1(T)$ modes, the trend of the DFPT frequencies as a function of temperature suggests a transition to an imaginary frequency at low temperature, but this is not yet observed in our calculations at ~80 K. This suggests that in DFPT, the transition temperature for these modes is very low, probably of the order of a few K, making its computation out of reach. The effective mass at the Fermi level is $m^* \approx 2.3$ for the π band and $m^* \approx 1.82$ for the π^* band. Their computation is detailed in Sec. S7 of Supplemental Material [23]. Thus, we consider $m^* = 2$ as the effective mass to compare with the model. In Figs. 2(c), 2(e), and 2(g), the EPC matrix elements for the three modes involved in the renormalization are presented as a function of the wavevector k. Let us first detail the predictions of our model based on the computed values of g_0 for each mode. Using Eq. (9), 54.5 meV are found for the RBM, 129.0 meV for the $A_1(L)$

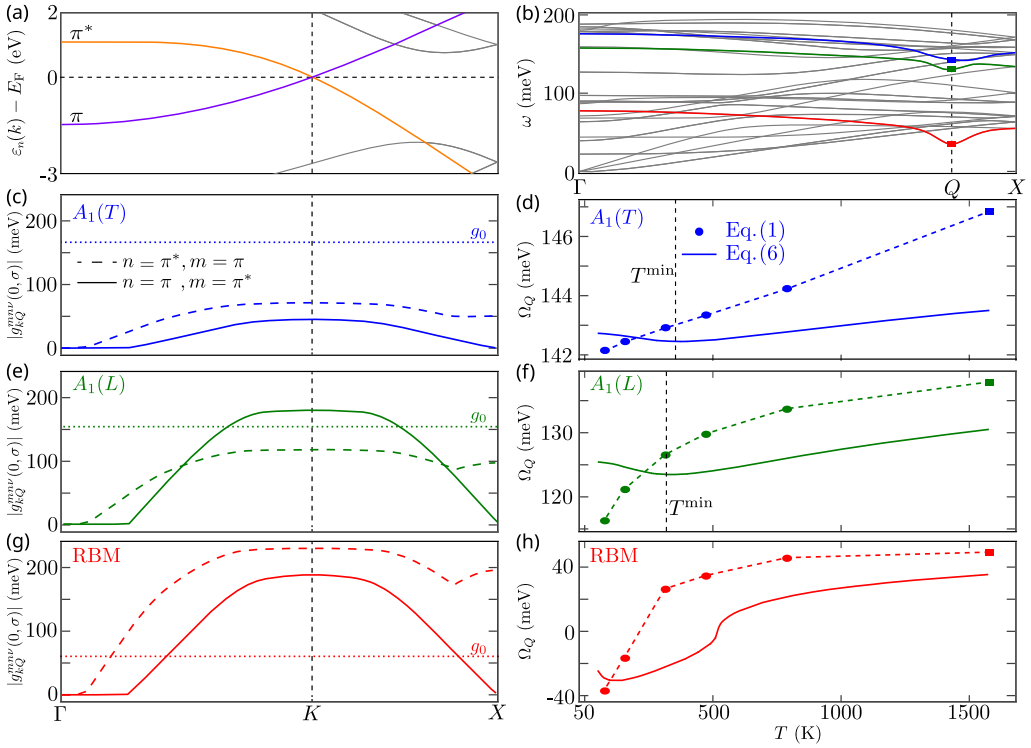

FIG. 2. The (a) electronic and (b) phonon band structures of the (3,3) carbon nanotube. The EPC matrix elements for $A_1(T)$ (c), $A_1(L)$ (e) and RBM (g). The dotted line is g_0 computed with Eq. (9). The renormalized phonon frequency for the three modes (d), (f) and (h). The solid line is computed with Eq. (6) while the dashed line is the DFPT reference. In the plot, imaginary frequencies are indicated as negative.

mode and 137.5 meV for the $A_1(T)$ mode, respectively. Comparing these values with $|g_{KQ}^{nm\nu}|$, we conclude that (i) the RBM is expected to soften as $|g_{KQ}^{nm\mathrm{RBM}}| \gg g_0$, (ii) the $A_1(L)$ mode needs further investigation as $|g_{KQ}^{nm\mathrm{A_1(L)}}| \sim g_0$, and (iii) the $A_1(T)$ mode should experience a negligible renormalization as $|g_{KQ}^{nm\mathrm{A_1(T)}}| \ll g_0$. Although $|g_{kQ}^{nm\nu}|$ assumes larger and smaller values than g_0, an appropriate comparison is to assess whether $|g_{kQ}^{nm\nu}|$ is larger or smaller than g_0 at the Fermi level, as detailed in Sec. S2 of Supplemental Material [23]. Furthermore, using Eq. (11), we predict that the renormalized frequency for the $A_1(T)$ mode should reach a minimum at 366 K. In Figs. 2(d), 2(f), and 2(h), the renormalized phonon frequency at $q = Q$ are shown as a function of temperature with a solid line for the $A_1(T)$ mode, the $A_1(L)$ mode, and RBM, respectively. Renormalized frequencies are computed using Eq. (6) and ω_Q with a cold smearing [38]. First, as expected, the RBM softens, with a transition temperature of approximately 525 K, refining the estimates of Refs. [35] and [39]. Next, we find that the $A_1(L)$ mode softens but remains positive throughout. The model of Eq. (11) predicts that the phonon frequency should reach a minimum around 330 K and then rises to a finite value at low temperature. Finally, as predicted, the $A_1(T)$ mode also softens but does not become imaginary. The temperature at which the renormalized frequency reaches a minimum is around 350 K, and the renormalization effect is even smaller. These observations validate the predictions of our model. Moreover, we can examine the effect of the adiabatic phonon frequency on the renormalization. Since the effective mass at the Fermi level is constant in the system, a lower adiabatic frequency appears to promote instability. Thus, while the RBM has a relatively low g_0 and does soften, the $A_1(L)$ and $A_1(T)$ modes have higher frequencies, leading to a larger g_0, which prevents softening. Furthermore, since $|g_{KQ}^{nm\mathrm{RBM}}| \gg g_0$, the transition occurs above room temperature, suggesting that the (3,3) CNT should experience a phase transition at room temperature in agreement with Ref. [35]. These small-diamater CNTs have been experimentally observed to be prone to instability at low temperature as detailed, for instance, in Ref. [40] for the (3,0) CNT.

To further validate our model, we computed the boron and strained gold chains, detailed in Sec. S8 of Supplemental Material [23], and further confirmed the results obtained from the theoretical model. For the longitudinal mode of the boron chain, the DFPT phonon frequency is 138.15 meV, the electron effective mass 0.67 and $|g_{KQ}^{nm\mathrm{LA}}| = 50$ meV. Using the values of ω_Q and m^* we obtain $g_0 = 240$ meV. Consequently, we do not expect the renormalized phonon frequency to become imaginary. Since $|g_{KQ}^{nm\mathrm{LA}}| \ll g_0$, we also expect the renormalized frequency to show a minimum at a temperature $T^{\min} = 350$ K. For the longitudinal mode of the strained gold chain, the DFPT frequency is 5.19 meV. The electron effective mass is 3, leading to $g_0 = 12.5$ meV. Given that $|g_{KQ}^{nm\mathrm{LA}}| \sim 70$ meV, we expect the renormalized phonon frequency to become imaginary. In both cases, Eq. (6) confirms the predictions of the model.

In conclusion, we have developed a simple model to demonstrate how instabilities due to KA are promoted by a low ω_Q and a large m^*. Using these physical quantities, we identify a threshold for the EPC strength above which the system becomes unstable at sufficiently low temperature. This threshold, g_0, can be compared with measured or computed EPC to easily estimate the stability of a system. We validate the results of this model through first-principles calculations on the (3,3) CNT, which confirmed our theoretical predictions. Furthermore, both the model and first-principles calculations indicate that although FS nesting alone is not sufficient to determine stability, it remains a necessary condition as the Kohn anomaly appears at a wave vector $\mathbf{Q} = 2\mathbf{k_F}$. This Letter emphasizes the dependence of Kohn anomalies on the intrinsic physical properties of one-dimensional systems and lays the groundwork for extending the model to two- and three-dimensional systems. The main challenge for such extensions is the complexity of solving the $\chi_{\mathbf{kq}}$ integral analytically in 2D and 3D. Moreover, finding realistic models to describe the 2D/3D Fermi surface accurately is nontrivial. If achieved, it would offer insight into whether similar conditions govern KA behavior in higher-dimensional materials.

Acknowledgments—E. M. acknowledges Victor Trinquet and Thomas P. van Waas for their assistance in solving the integrals in Sec. S4 of Supplemental Material [23]. S. P. and G.-M. R. acknowledge support from the Fonds de la Recherche Scientifique de Belgique (FRS-FNRS) and by the Walloon Region in the strategic axe FRFS-WEL-T. J.-C. C. acknowledges financial support from the Fédération Wallonie-Bruxelles through the ARC project "DREAMS" (No. 21/26-116), from the EOS project "CONNECT" (No. 40007563), and from the Belgium FRS-FNRS through the research project (No. T.029.22F). Computational resources have been provided by the supercomputing facilities of the Université catholique de Louvain (CISM/UCL) and the Consortium des Équipements de Calcul Intensif en Fédération Wallonie Bruxelles (CÉCI) funded by the Fond de la Recherche Scientifique de Belgique (F.R.S.-FNRS) under convention 2.5020.11 and by the Walloon Region. The present research benefited from computational resources made available on Lucia, the Tier-1 supercomputer of the Walloon Region, infrastructure funded by the Walloon Region under the Grant Agreement No. 1910247.

Data availability—A record is also available on the Materials Cloud Archive at [41], containing the

ab initio input files used to generate the data presented in this work and the Python scripts employed to reproduce Figs. 1 and 2.

[1] W. Kohn, Image of the Fermi surface in the vibration spectrum of a metal, Phys. Rev. Lett. **2**, 393 (1959).

[2] B. N. Brockhouse, K. R. Rao, and A. D. B. Woods, Image of the Fermi surface in the lattice vibrations of lead, Phys. Rev. Lett. **7**, 93 (1961).

[3] B. N. Brockhouse, T. Arase, G. Caglioti, K. R. Rao, and A. D. B. Woods, Crystal dynamics of lead. I. Dispersion curves at 100°K, Phys. Rev. **128**, 1099 (1962).

[4] Y. Nakagawa and A. D. B. Woods, Lattice dynamics of niobium, Phys. Rev. Lett. **11**, 271 (1963).

[5] S. H. Koenig, Kohn effect in Na and other metals, Phys. Rev. **135**, A1693 (1964).

[6] A. Q. R. Baron, H. Uchiyama, Y. Tanaka, S. Tsutsui, D. Ishikawa, S. Lee, R. Heid, K.-P. Bohnen, S. Tajima, and T. Ishikawa, Kohn anomaly in MgB_2 by inelastic x-ray scattering, Phys. Rev. Lett. **92**, 197004 (2004).

[7] P. Aynajian, T. Keller, L. Boeri, S. M. Shapiro, K. Habicht, and B. Keimer, Energy gaps and Kohn anomalies in elemental superconductors, Science **319**, 1509 (2008).

[8] B. M. Powell, P. Martel, and A. D. B. Woods, Lattice dynamics of niobium-molybdenum alloys, Phys. Rev. **171**, 727 (1968).

[9] J. Kulda, H. Kainzmaier, D. Strauch, B. Dorner, M. Lorenzen, and M. Krisch, Overbending of the longitudinal optical phonon branch in diamond as evidenced by inelastic neutron and x-ray scattering, Phys. Rev. B **66**, 241202 (2002).

[10] R. E. Peierls, *Quantum Theory of Solids* (Oxford University Press, New York, 1955).

[11] X. Zhu, Y. Cao, J. Zhang, E. W. Plummer, and J. Guo, Classification of charge density waves based on their nature, Proc. Natl. Acad. Sci. U.S.A. **112**, 2367 (2015).

[12] M. D. Johannes and I. I. Mazin, Fermi surface nesting and the origin of charge density waves in metals, Phys. Rev. B **77**, 165135 (2008).

[13] J. Tidholm, O. Hellman, N. Shulumba, S. I. Simak, F. Tasnádi, and I. A. Abrikosov, Temperature dependence of the Kohn anomaly in bcc Nb from first-principles self-consistent phonon calculations, Phys. Rev. B **101**, 115119 (2020).

[14] J. Berges, N. Girotto, T. Wehling, N. Marzari, and S. Poncé, Phonon Self-Energy Corrections: To Screen, or Not to Screen, Phys. Rev. X **13**, 041009 (2023).

[15] F. Caruso, M. Hoesch, P. Achatz, J. Serrano, M. Krisch, E. Bustarret, and F. Giustino, Nonadiabatic Kohn anomaly in heavily boron-doped diamond, Phys. Rev. Lett. **119**, 017001 (2017).

[16] N. Girotto and D. Novko, Dynamical renormalization of electron-phonon coupling in conventional superconductors, Phys. Rev. B **107**, 064310 (2023).

[17] X. Gonze and C. Lee, Dynamical matrices, Born effective charges, dielectric permittivity tensors, and interatomic force constants from density-functional perturbation theory, Phys. Rev. B **55**, 10355 (1997).

[18] X. Gonze, First-principles responses of solids to atomic displacements and homogeneous electric fields: Implementation of a conjugate-gradient algorithm, Phys. Rev. B **55**, 10337 (1997).

[19] M. Calandra, G. Profeta, and F. Mauri, Adiabatic and nonadiabatic phonon dispersion in a Wannier function approach, Phys. Rev. B **82** (2010).

[20] F. Giustino, Electron-phonon interactions from first principles, Rev. Mod. Phys. **89**, 015003 (2017).

[21] A. Marini, Dynamical electron-phonon vertex correction, arXiv:2501.01866.

[22] G. Stefanucci and E. Perfetto, Exact formula with two dynamically screened electron-phonon couplings for positive phonon-linewidths approximations, Phys. Rev. B **111** (2025).

[23] See Supplemental Material at http://link.aps.org/supplemental/10.1103/x69r-8fw1 for details on the 1D model, the analytical computation of the polarizability at $T = 0$ K, its temperature-dependent approximations, and on the EPC matrix element value used for comparison with theory and other first-principles examples, which include Refs. [15,24].

[24] L. He, F. Liu, J. Li, G.-M. Rignanese, and A. Zhou, First-principles investigation of monatomic gold wires under tension, Comput. Mater. Sci. **171**, 109226 (2020).

[25] J.-M. Lihm, S. Poncé, and C.-H. Park, Self-consistent electron lifetimes for electron-phonon scattering, Phys. Rev. B **110**, L121106 (2024).

[26] P. Giannozzi, S. Baroni, N. Bonini, M. Calandra, R. Car, C. Cavazzoni, D. Ceresoli, G. L. Chiarotti, M. Cococcioni, I. Dabo *et al.*, QUANTUM ESPRESSO: a modular and open-source software project for quantum simulations of materials, J. Phys. Condens. Matter **21**, 395502 (2009).

[27] P. Giannozzi, O. Andreussi, T. Brumme, O. Bunau, M. B. Nardelli, M. Calandra, R. Car, C. Cavazzoni, D. Ceresoli *et al.*, Advanced capabilities for materials modelling with QUANTUM ESPRESSO, J. Phys. Condens. Matter **29**, 465901 (2017).

[28] P. Giannozzi, O. Baseggio, P. Bonfà, D. Brunato, R. Car, I. Carnimeo, C. Cavazzoni, S. de Gironcoli, P. Delugas, F. Ferrari Ruffino *et al.*, Quantum ESPRESSO toward the exascale, J. Chem. Phys. **152**, 154105 (2020).

[29] F. Giustino, M. L. Cohen, and S. G. Louie, Electron-phonon interaction using Wannier functions, Phys. Rev. B **76**, 165108 (2007).

[30] S. Poncé, E. Margine, C. Verdi, and F. Giustino, EPW: Electron-phonon coupling, transport and superconducting properties using maximally localized Wannier functions, Comput. Phys. Commun. **209**, 116 (2016).

[31] H. Lee, S. Poncé, K. Bushick, S. Hajinazar, J. Lafuente-Bartolome, J. Leveillee, C. Lian, J. Lihm, F. Macheda, H. Mori *et al.*, Electron–phonon physics from first principles using the EPW code, npj Comput. Mater. **9**, 156 (2023).

[32] M. van Setten, M. Giantomassi, E. Bousquet, M. Verstraete, D. Hamann, X. Gonze, and G.-M. Rignanese, The PseudoDojo: Training and grading a 85 element optimized norm-conserving pseudopotential table, Comput. Phys. Commun. **226**, 39 (2018).

[33] N. Marzari, A. A. Mostofi, J. R. Yates, I. Souza, and D. Vanderbilt, Maximally localized Wannier functions: Theory and applications, Rev. Mod. Phys. **84**, 1419 (2012).

[34] G. Pizzi, V. Vitale, R. Arita, S. Blügel, F. Freimuth, G. Géranton, M. Gibertini, D. Gresch, C. Johnson, and T. Koretsune, Wannier90 as a community code: new features and applications, J. Phys. Condens. Matter **32**, 165902 (2020).

[35] D. Connétable, G.-M. Rignanese, J.-C. Charlier, and X. Blase, Room temperature peierls distortion in small diameter nanotubes, Phys. Rev. Lett. **94**, 015503 (2005).

[36] R. Barnett, E. Demler, and E. Kaxiras, Electron-phonon interaction in ultrasmall-radius carbon nanotubes, Phys. Rev. B **71**, 035429 (2005).

[37] N. Wang, Z. Tang, G. Li, and J. Chen, Single-walled 4 Å carbon nanotube arrays, Nature (London) **408**, 50 (2000).

[38] N. Marzari, D. Vanderbilt, A. De Vita, and M. C. Payne, Thermal contraction and disordering of the Al(110) surface, Phys. Rev. Lett. **82**, 3296 (1999).

[39] K.-P. Bohnen, R. Heid, H. J. Liu, and C. T. Chan, Lattice dynamics and electron-phonon interaction in (3,3) carbon nanotubes, Phys. Rev. Lett. **93**, 245501 (2004).

[40] B. Zhang, T. Zhang, J. Pan, T. Chow, A. Aboalsaud, Z. Lai, and P. Sheng, Peierls-type metal-insulator transition in carbon nanostructures, Carbon **172**, 106 (2021).

[41] E. Marazzi, S. Poncé, J.-C. Charlier, and G.-M. Rignanese, Importance of non-adiabatic effects on Kohn anomalies in 1D metals, Materials Cloud Archive (2025), 10.24435/materialscloud:yx-x1.